Impact of glycan nature on structure and viscoelastic properties of glycopeptide hydrogels

Jonas Proksch[1], Marlene C. S. Dal Colle[1,2], Frederick Heinz[1], Robert F. Schmidt[3], Jacqueline Gottwald[4], Martina Delbianco[2], Bettina G. Keller[3], Michael Gradzielski[3], Ulrike Alexiev[4] and Beate Koksch[1,*]

1 Institute of Chemistry and Biochemistry, Freie Universität Berlin, Arnimallee 20-22, 14195 Berlin, Germany
2 Department of Biomolecular Systems, Max Planck Institute of Colloids and Interfaces, Am Mühlenberg 1, 14476 Potsdam, Germany
3 Stranski-Laboratorium für Physikalische und Theoretische Chemie, Institut für Chemie, Technische Universität Berlin, Straße des 17. Juni 124, 10623 Berlin, Germany
4 Department of Physics, Freie Universität Berlin, Arnimallee 14, 14195 Berlin, Germany
* Author to whom correspondence should be addressed; electronic mail: beate.koksch@fu-berlin.de

Graphical Abstract

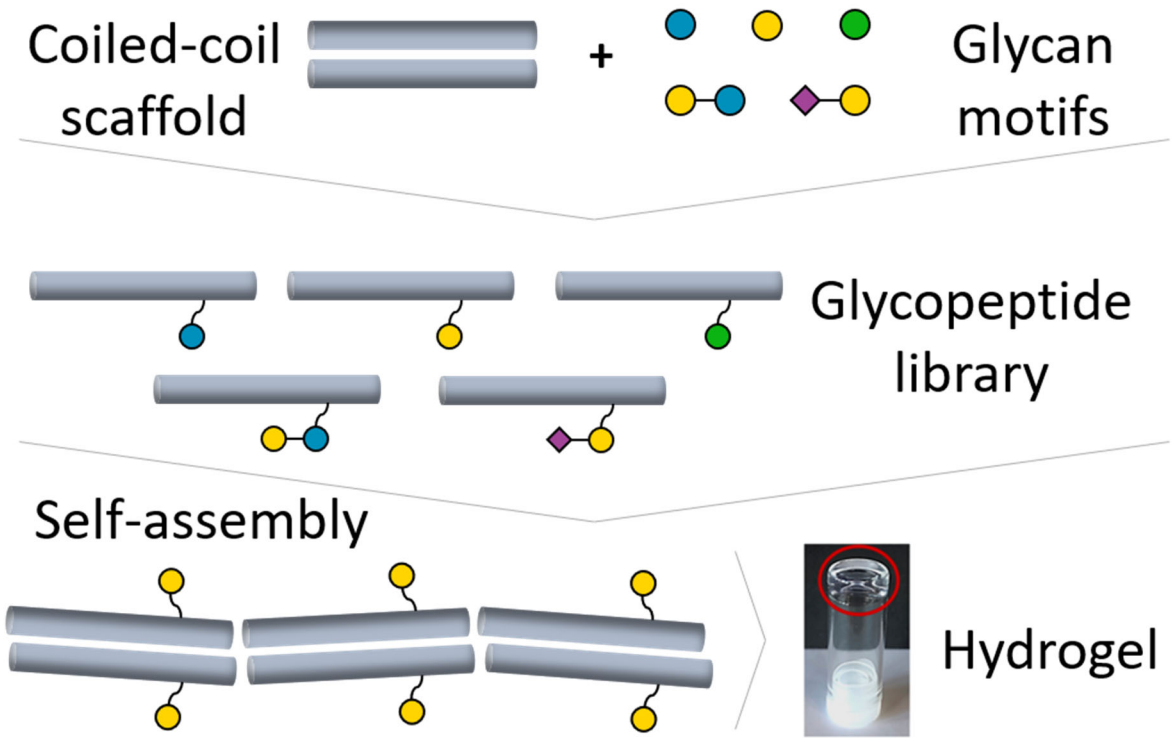

Key words

mucus, glycopeptide library, peptide self-assembly, peptide hydrogels, rheology

Abstract

Mucus is a complex biological hydrogel that acts as a barrier for almost everything entering or exiting the body. It is therefore of emerging interest for biomedical and pharmaceutical applications. Besides water, the most abundant components are the large and densely glycosylated mucins, a family of glycoproteins with sizes of up to 20 MDa and a carbohydrate content of up to 80 wt%. Here, we designed and explored a library of glycosylated peptides to deconstruct the complexity of mucus. By using the well characterised hFF03 coiled-coil system as a hydrogel-forming peptide scaffold, we systematically probed the contribution of single glycans to the secondary structure as well as the formation and the viscoelastic properties of the resulting hydrogels. We show that glycan-decoration does not affect α-helix and coiled-coil formation while it alters gel stiffness. By using oscillatory macrorheology, dynamic light scattering microrheology and fluorescence lifetime-based nanorheology, we characterised the glycopeptide materials over several length scales. Molecular simulations revealed that the glycosylated linker may extend into the solvent, but more frequently interacts with the peptide, thereby likely modifying the stability of the self-assembled peptide fibres. The results of this systematic study highlight the interplay between glycan structure and hydrogel properties and may guide the development of synthetic mucus mimetics.

Introduction

Mucus is a biological hydrogel at the interface between body and environment. It lines every wet epithelial surface and forms a highly selective barrier. While it allows for the exchange of nutrients and gases, noxious agents and pathogens are entrapped. Mucus also serves to hydrate the underlying mucosa and acts as a lubricant.[1] Moreover, it hosts a remarkably diverse microbial community essential to human health.[2] Primarily responsible for many of these properties are the major structural components of mucus, the mucins. Mucins are a class of over 20 mucin-type high molecular weight glycoproteins, all belonging to the *MUC* gene family. The mucin molecule is composed of a rigid and extended protein backbone with a variable number of tandem repeats rich in proline, threonine and serine (PTS domains), as well as cysteine-rich regions at the two termini and between PTS domains.[3] The PTS domains are usually densely *O*-glycosylated with branched oligosaccharide chains forming a structure that resembles a bottlebrush. The semi-flexible protein backbone and the highly hydrophilic nature of the *O*-glycans contribute to the biophysical properties of mucus. The hydrogel character of mucus is mainly arising from entanglement of mucin fibres that form a three-dimensional network as well as non-covalent interactions and disulfide bonds. While the viscoelastic properties can vary drastically depending on the organ of origin and the state of health or disease, the storage modulus G' of healthy mucus is in the range of 1-10 Pa for probing frequencies above 1 Hz. The mesh size of mucus is also highly heterogeneous and can vary from 20 to 1800 nm across different organs.[4]

In order to understand this very complex material and its role in the pathways of many infectious and chronic diseases there is a need for artificial mucin-like systems that mimic some of the properties and functions of native mucus. Ribbeck et al. have shown recently that single glycans are inhibitors of virulence in *Vibrio cholerae*.[5] Well-defined synthetic model systems that display single glycans can thus help identify such core structures and elucidate their role in the onset of disease, for example by performing binding studies with pathogens. It is however not trivial to mimic and investigate these intricate structures based on chemically synthesised materials and current research often relies on reconstituted mucins of animal origins. Commercially available mucins are for example bovine submaxillary mucin (BSM) or porcine gastric mucin (PGM).[6] All these samples differ largely in their

molecular, mesoscopic, and macroscopic properties depending on the donor species and their state of health or disease.[7] Moreover, for commercial mucins the isolation procedure often changes the physicochemical properties irreversibly, leading to different characteristics and structure after rehydration of the mucin.[8,9] Hence there is a great need for a chemically defined synthetic model mimicking key properties of mucus that would enable systematic studies based on reproducible (starting) conditions. Recently, different polymerisation approaches have been used to mimic mucins and their hydrogels.[10,11] We chose to employ a peptide-based approach. The advantage that this system offers lies in its modularity, well-defined structure, and easy synthetic access. Through solid phase peptide synthesis (SPPS) access to well-defined structures is possible in a relatively short amount of time. This backbone can then be decorated with synthetic glycans obtained via chemical or chemoenzymatic syntheses.

Prior work from our group focused on the defined presentation of glycans using self-assembling peptide scaffolds[12,13] and the functionalisation of peptide hydrogels with cell adhesion motives and mannose[14]. Here we extend these systems to include decoration with mucin-relevant glycans and characterise hydrogel properties on different length scales, focusing on rheology. We used several experimental techniques to investigate the physicochemical features that characterise a mucus-inspired hydrogel over a range of length scales and how they change upon introduction of single glycans. Oscillatory shear rheology is used to obtain macroscopic bulk properties, such as the storage (G') and loss modulus (G'') associated with the elastic and viscous properties, respectively, on length scales from 0.1-10 mm. Dynamic light scattering (DLS) microrheology yields insight into the microstructural organisation on length scales from 0.01-1 μm. By following the scattering of tracer particles, one can gain their mean squared displacement (MSD) and diffusion coefficient. Moreover, we used a recently established nanorheology technique that translates the fluorescence lifetime of a molecular rotor dye (FMR) into information about its immediate environment (<10 nm). This technique can thus give an idea of how small analytes move within the hydrogel. Finally, we aimed to bridge the gap between macro and nanorheology by DLS microrheology that can give overlapping information with both of the other techniques. Additionally, we used molecular dynamics simulations to elucidate the dynamics and the structure of the glycosylated linker relative to the peptide.

Design of the glycopeptide library

The coiled-coil structure is widely observed in nature and has drawn substantial interest due to its clear sequence-to-structure relationship and ease of tunability.[12,13,15,16] It has been used to create and study higher order assemblies[17] and for a multitude of biomedical applications[18-21]. The hFF03 (hydrogelating fibre-forming) peptide was developed in our group and used as a tuneable extracellular matrix mimic by decoration with cell adhesion motives or carbohydrate ligands.[14] We chose to use this scaffold for its synthetic accessibility and straightforward decoration leading to defined glycan-peptide conjugates.

hFF03 is a 26-residue peptide which forms α-helical coiled-coil dimers of 4 nm length (Figure 1a). The coiled-coil dimers subsequently self-assemble into fibrils via dimer-to-dimer contacts in which the N-terminus of one coiled-coil dimer forms a network of salt-bridges and hydrogen bonds to the C-terminus of an adjacent coiled-coil dimer. The stability of this dimer-to-dimer contact significantly influences the viscoelastic properties of the hydrogel.[22] In this study we used *ortho*-aminobenzoic acid as N-terminal label. The fibrils formed by this system are highly dynamic with a persistence length of approximately 10 nm and a diameter of approximately 2.6 nm.[14]

This well-characterised system is suitable for studying the contribution of conjugated single components, such as monosaccharides, to the viscoelastic properties of the hydrogel. Therefore, this peptide backbone was systematically decorated with different single glycans (Figure 1b), and the properties of the resulting hydrogels were studied under different conditions. The saccharides we chose (galactose, sialylated galactose) were derived from glycan motives found in native mucins (MUC5AC, MUC5B, MUC2)[23] and complemented by other glycan motives of interest (glucose, mannose, lactose) for a systematic study of the structure-property relationship.

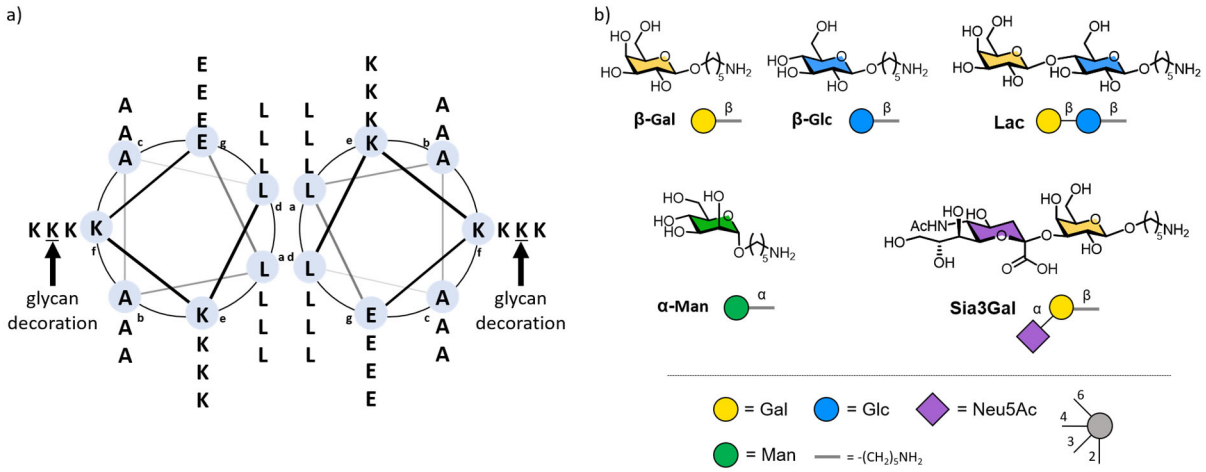

Figure 1: a) Helical wheel projection of the hFF03 peptide; b) Carbohydrate motifs used for decoration of the peptide backbone.

Materials and Methods

Preparation of Peptide Conjugate Hydrogels

The synthesis of the glycan peptide conjugates can be divided into three parts. Firstly, the glycan building block was synthesised. Next, the peptide was synthesised using solid phase peptide synthesis (SPPS). Lastly, the peptide, while still on-resin, was selectively deprotected at lysine residue 18 and the glycan attached at this point.

Synthesis of glycans

The glycans were synthesised according to published procedures either via automated glycan assembly (AGA)[24,25], solution phase synthesis[26,27] or chemoenzymatic synthesis (for sialylated glycans)[28,29]. The structures carry an aminopentanol linker at the reducing end to be used for conjugation to the peptide. Details and analytical data can be found in the SI.

Synthesis of peptides

Peptides were synthesised with a microwave-assisted automated synthesiser Liberty Blue (CEM, Matthews, NC, USA) using standard fluorenylmethoxycarbonyl (Fmoc) chemistry with diisopropylcarbidiimide (DIC) as the activating agent and ethyl 2-cyano-2-(hydroxyamino)acetate (Oxyma Pure) as additive. The synthesis was performed on a 0.1 mmol scale on Fmoc-Leu-NovaSyn TGA (0.19 mmol/g loading) resin from Novabiochem. A 5-fold excess of amino acid (Carbolution) was used in each coupling. Glutamic acid was protected by *tert*-butyl ester (*t*Bu) and lysine by *tert*-butoxycarbonyl (Boc), except for the lysine incorporated at position 18 which was

protected by monomethoxytrityl (Mmt) (purchased from CEM) for orthogonal deprotection and subsequent functionalisation. Undecorated hFF03 peptide was cleaved from the resin by treatment with a mixture of trifluoroacetic acid (TFA), triisopropylsilane (TIPS) and water (95:2.5:2.5 v/v; 5 mL/g of resin) for 2 h at room temperature.

Glycan decoration of peptides

After full-length synthesis, the Mmt protected lysine residue at position 18 was deprotected selectively using a mixture of dichloromethane, trifluoroethanol and acetic acid (7:2:1, v/v; 1x 30 min, 1x 2.5 h). The freed ε-amino function was then converted into a carboxy function by treatment with a solution of glutaric anhydride (5 equiv.) and DIPEA (catalytic) in DMF. Lastly, the carboxy function was activated with a solution of HATU (2 equiv.) and DIPEA (2 equiv.) in DMF and a solution of the respective glycan (1 equiv.) in DMF was added. Full cleavage of the peptides was achieved by treating the resin with a mixture of TFA, dichloromethane, TIPS and water (50:45:2.5:2.5 v/v) for 3x 30 min. After filtration, volatiles were evaporated and the peptides precipitated in cold diethyl ether, centrifuged, dissolved in water and lyophilised. Purification was performed using preparative RP-HPLC.

Exchange of TFA adduct

The use of TFA for cleavage from the resin and as an additive in eluents for preparative HPLC inevitably yields peptides as TFA adducts. In order to exchange the trifluoroacetic acid anion against chloride, peptides were dissolved in water at a concentration of 0.5 mM. To this solution 6 M HCl was added to give a final concentration of 7.5 mM HCl. It was stirred for 1 minute at room temperature and then lyophilised. The procedure was repeated five times in total.

Sample Preparation

Purified peptides were dissolved in 1,1,1,3,3,3-hexafluoroisopropanol (HFIP) at roughly 1 mg per 100 µL and sonicated for 15 minutes. An aliquot of the stock solution was evaporated in a gentle stream of nitrogen gas and the resulting peptide film dissolved in 1 mL of Dulbecco's phosphate buffered saline (DPBS) containing 6 M guanidine hydrochloride. Absorbance of this solution at 320 nm was measured with a Varian Cary 50 photometer (Varian Medical Systems, Palo Alto, CA, USA). The concentration was then calculated using a calibration curve of dipeptide H-Abz-Gly-OH (see SI for details).

From the HFIP peptide stock solutions of known concentration appropriate amounts were then evaporated using a gentle flow of nitrogen gas, the resulting peptide residue then dissolved as described at the respective experiment section.

Circular Dichroism Spectroscopy

Circular dichroism (CD) spectra of hydrogel samples were recorded using demountable Quartz Suprasil cuvettes (Hellma Analytics, Mühlheim, Germany) with a path length of 0.1 mm. Measurements were performed at 37 °C and a mean of three measurements was taken. Spectra were background-corrected by subtraction of solvent/buffer spectra at 37 °C and normalised by path length, molar concentration and number of amide bonds.

Samples were prepared by dissolving peptides in either DPBS (w/o Ca^{2+}, Mg^{2+}, Sigma) or water for pH-dependent experiments. In the case of water, pH was adjusted to the desired pH by addition of 1 M aqueous NaOH or HCl

and the remaining volume until desired concentration filled up using 150 mM NaCl solution to account for ion strength. Samples were vortexed for 10 s and incubated for 16 h at room temperature (19-21°C).

Rheology

Macrorheology

All macrorheological measurements were performed on an Anton Paar MCR 502 WESP temperature-controlled rheometer in strain-imposed mode at 37 °C. A chromium oxide-coated cone-plate measurement system was used with a diameter of 25 mm, a cone truncation (gap width) of 48 µm and a cone angle of 1°. The temperature was set using a Peltier measuring system combined with a Peltier hood to ensure a minimized temperature gradient throughout the sample. For each measurement, 120 µL of sample is loaded onto the plate, the cone is lowered slowly and any excess sample is trimmed before starting the measurement.

In a preliminary amplitude sweep (AS), the strain amplitude γ_0 was varied between 0.1 and 10% at a constant frequency of 6.3 rad/s to determine the linear viscoelastic regime. For the frequency sweeps, the strain amplitude was kept fixed at 5% (value determined from AS) and the oscillation frequency varied between 0.05 and 50 Hz, which corresponds to 0.314 and 314 rad/s. For each sample, the frequency was first varied in increasing and then in decreasing order to check for hysteresis effects. Since no systematic hysteresis effects were observed, only the increasing frequency data are considered below. At very high frequencies, artefacts can occur, leading to unrealistic values for G' and G''. Therefore, only frequencies $\omega \leq 52.4$ rad/s are considered.

In addition, continuous shear experiments were performed, where the shear rate was varied between 0.01 and 100 s^{-1}, first in increasing and then in decreasing order. New data points are created when the measured viscosity is constant within 1% error for 2 s. This means that the overall measurement time varies from sample to sample.

Samples were prepared by dissolving peptides in either DPBS (w/o Ca^{2+}, Mg^{2+}, Sigma) or water. pH was adjusted by addition of 1 M aqueous NaOH or HCl and the remaining volume until the desired concentration filled up using 150 mM NaCl solution to account for ion strength. Samples were vortexed for 10 s and incubated for 16 h at room temperature (19-21°C).

DLS-Microrheology

DLS measurements were performed on a Litesizer 500 instrument from Anton Paar (Graz, Austria), equipped with a 40 mW semiconductor laser diode with a wavelength of $\lambda = 658$ nm at a fixed scattering angle of $\theta = 175°$. Using the refractive index of DPBS buffer $n = 1.3318$, the magnitude of the scattering vector scattering vector is $q = 4\pi n/\lambda \sin(\theta/2) = 0.025$ nm^{-1}. A 3 x 3 mm low volume quartz cuvette was used at a constant temperature of 25 °C. Three separate 30 min measurements were performed and averaged. The intensity-intensity autocorrelation function $g^{(2)}(\tau)$ can be related to the mean-squared displacement $\langle \Delta r^2(\tau) \rangle$ (MSD) of the tracer particles through the intermediate scattering function [9]

$$g^{(1)}(\tau) = exp\left(\frac{-q^2\langle \Delta r^2(\tau)\rangle}{6}\right) \quad (1)$$

Assuming that the sample is ergodic, $g^{(1)}(\tau)$ is related to $g^{(2)}(\tau)$ through the Siegert relation[10,11]

$$g^{(2)}(\tau) = 1 + \beta\left|g^{(1)}(\tau)\right|^2 \quad (2)$$

where $\beta = g^{(2)}(\tau \rightarrow 0)$ is determined by fitting a stretched exponential to $g^{(2)}(\tau)$ for 8.8 x 10^{-7} s < τ < 1.41 x 10^{-5} s. Inaccuracies in the determination of β can influence the y-intercept of the MSD. Since by definition, $\langle \Delta r^2(\tau = 0) \rangle = 0$, we perform a linear fit of the MSD in the range $10^{-6} < \tau < 5$ x 10^{-6} s and subtract the y-intercept. The MSD of tracer particles embedded in a viscoelastic fluid can be converted to the complex modulus $G^*(\omega)$ using the generalized Stokes-Einstein equation [12,13]

$$G^*(\omega) = \frac{kT}{\pi a i \omega \mathcal{F}_u\{\langle \Delta r^2(\tau) \rangle\}} \quad (3)$$

where a is the tracer particle radius, i is the imaginary unit and $\mathcal{F}_u\{\langle \Delta r^2(\tau) \rangle$ denotes the unilateral Fourier transform of the MSD. Instead of performing a numerical Fourier transform, we adopt the method introduced by Mason *et al.*, where the MSD is described by a local power law followed by an analytical Fourier transformation [14,15]. The power law exponent $\alpha(\omega)$ is determined from the logarithmic time derivative of the MSD:

$$\alpha(\omega = 1/\tau) = \frac{\partial \, ln\langle \Delta r^2(\tau) \rangle}{\partial \, ln \, \tau} \quad (4)$$

where we have used that the frequency is the inverse of the lag time. In viscoelastic fluids, $0 < \alpha < 1$ (0 corresponds to a purely elastic solid and 1 corresponds to a purely viscous liquid). Analytical Fourier transform of the local power law, together with Eq. 7 yields

$$G'(\omega) = G(\omega) \, cos[\pi\alpha(\omega)/2] \quad (5)$$

$$G''(\omega) = G(\omega) \, sin[\pi\alpha(\omega)/2] \quad (6)$$

where

$$G(\omega) = \frac{kT}{\pi a \langle \Delta r^2(1/\omega) \rangle \Gamma[1 + \alpha(\omega)]} \quad (7)$$

Here, $\Gamma(z) = \int_0^\infty x^{z-1} e^{-x} dx$ is the Gamma function.

Samples were prepared by dissolving peptides in a suspension of Cy3 labelled polystyrene beads (Nanocs, hydrodynamic diameter = 216.9 nm) in DPBS (w/o Ca^{2+}, Mg^{2+}, Sigma). Samples were vortexed for 10 s and incubated for 16 h at room temperature (19-21°C).

Spectroscopy

Time-resolved Fluorescence Spectroscopy in FLIM mode

The fluorescence lifetime curves of Cy3 (sulfo-Cyanine3 maleimide (Lumiprobe, Germany)) in the peptide hydrogel and in different sucrose/water mixtures were recorded in a home-built setup combining time-correlated single photon counting (TCSPC) and confocal laser scanning microscopy as previously described [30,31] to allow the measurement of small samples of 25-50 µl hydrogel. The setup consists of an inverted microscope (IX71,

Olympus, Shinjuku, Tokio, Japan), a tunable ps-supercontinuum white light laser (SuperK Extreme EXU-3, NKT Photonics, Birkerød, Denmark), a confocal scanning unit (DCS120, Becker & Hickl, Germany), a hybrid PMT detector (HPM-100-40, Becker & Hickl, Germany), and a TCSPC-module (SPC150, Becker & Hickl, Germany). FLIM images were recorded by the SPCM software (Becker & Hickl, Germany) using a 60x objective (water, UPLSAPO60XW, Olympus, Japan), resulting in a total field of view with 300 µm side length. An acousto-optical tunable filter (SELECT UV-VIS, NKT Photonics, Denmark) was used to select the fluorescence excitation wavelengths from the white light laser beam. The laser repetition rate was set to 19.5 MHz. Cy3 was excited at 530 nm and the fluorescence emission was spectrally selected by a long-pass filter (> 545 nm, Chroma, Rockingham, USA). A notch filter (Semrock, USA) removed the residual scattered excitation light. The TCSPC-module sorts the detected fluorescence photons into 1024 time channels with a channel width of 19.97 ps. The instrument response function (IRF) of the system was less than 100 ps (FWHM). To analyse the fluorescence decay traces, the decay histograms from all pixels in the FLIM image were summed up. Subsequently, the fluorescence decay curve was fitted by a multi-exponential model function after deconvolution using a calculated IRF

$$I(t) = \sum_i^n \alpha_i \, e^{-t/\tau_i}, \tag{8}$$

with n the total number of decay components, α_i the amplitude and τ_I the fluorescence lifetime of the i-th component [32,33] .The population-weighted mean fluorescence lifetime τ_{mean} was calculated by

$$\tau_{mean} = \sum_i^n \beta_i \, \tau_i, \tag{9}$$

with β_i being the fractional amplitude (population amplitude) of the i-th component with

$$\beta_i = \frac{\alpha_i \tau_i}{\sum_i^n \alpha_i \tau_i}. \tag{10}$$

Viscosity Dependence of Cy3 Fluorescence Decay Traces

Cy3 was investigated by time-resolved fluorescence spectroscopy in sucrose/water mixtures ranging from 0 % to 70 % (w/w) sucrose. The obtained fluorescence decay traces were fitted by Eq.(8 and the mean fluorescence lifetimes were calculated by Eq. (9. The viscosity dependence was analysed as previously described for a cyanine 3 dye[30]. Briefly, the viscosity values were taken from ref.[34] at the different sucrose concentrations. The mean fluorescence lifetimes as a function of viscosity were evaluated by an extended Förster-Hoffmann equation, which includes a temperature-dependent activation energy for dye isomerization:

$$\bar{\tau}_{pop} = \left(\frac{1}{C\eta^{\alpha} + \frac{1}{A_{max}}} \cdot e^{-\frac{E_a}{kT}} + k_f + k_x \right)^{-1}. \tag{11}$$

C is a constant and $1/A_{max}$ indicates that τ does not go to zero at zero viscosity, k_f and k_x are the rate of fluorescence and all other non-radiative rates, respectively, from the excited to the ground state [30,35].

Hydrogel preparation for nanoviscosity studies using Cy3

Peptide was dissolved in 50 µl aliquots at a concentration of 0.5% (w/v) in DPBS (w/o Ca^{2+}, Mg^{2+}, Sigma) which included 0.5 µM Cy3, vortexed for ten seconds, gently mixed by pipetting and again vortexed for ten seconds. After 1-2 h the solution was again carefully mixed by pipetting to allow homogeneous hydrogel formation and was used for Cy3 fluorescence lifetime measurements the following day. To follow the viscosity increase during peptide hydrogel formation, we measured the Cy3 fluorescence lifetime at different time delays after initial mixing with buffer.

Molecular Dynamics Simulations

Simulations

The initial coiled-coil structure was built with the sequence LKKELAA-LKKELAA-LKKELAA-LKKEL using the web tool CCBuilder2.0 by Derek Woolfson.[36] Lysine residues and amino group of the *ortho* aminobenzoic acid are protonated (charge+1), glutamate residues and the C-terminus are deprotonated (charge -1), corresponding to the expected protonation at pH 7. A single coiled-coil dimer has a total charge of +8. The *ortho* aminobenzoic acid at the N-terminus, the anhydride linker and the C5 chain were added manually with Pymol. The corresponding force field parameters were calculated with AmberTools[37], with the gas charge calculation method. The glycans α-mannose, β-glucose, β-galactose and their force field parameters were added with the doGlycans[38]. 32 coiled-coil dimers of α-mannose-hFF03, β-glucose-hFF03 or β-galactose-hFF03 were solvated in TiP4P water with 0.1 M NaCl in a cubic box with 20 nm box length, corresponding to roughly a 4% polymer mass fraction. 256 Cl^- anions were added to generate a neutral simulation box.

MD simulations were carried out with Gromacs2021+CUDA on the Curta cluster system[39] with the Amber99SB-ILDN force field[40]. After energy minimisation and relaxation in NVT and NPT ensemble, the simulations are carried out in the NPT-ensemble. The temperature was maintained at T = 300 K using the velocity-rescale thermostat with a coupling constant of 0.1 ps. The pressure was maintained at 1 bar using the Parinello-Rahman barostat with a coupling constant of 2 ps. The simulation uses a leap frog integrator with 2 fs per step and periodic boundary conditions in all three spatial direction. Covalent bonds to hydrogen atoms were constraint using the LINCS algorithm. Coordinates were written to file every 20 ps. A simulation of 50 ns length was conducted for each of the three systems.

The force field and all input files for the simulations are available via the code repository: https://github.com/bkellerlab/hFF03_hydrogels.

Analysis

To analyse the relative positions of the glycans to the coiled-coil backbone we consider the backbone of a single coiled-coil to be linear. This allows the usage of trigonometry to specify the position of the glycan. First, we create a back-bone vector $\vec{v}$ from the N-terminus to the C-terminus. To obtain a vector going through the centre of the coiled-coil we use the average of the Cα atoms for both α-helices of the coiled-coil. We specifically use the Cα atoms of the first and last lysine since these always are oriented towards the centre of the coiled-coil (lysine zipper). For the glycan we use the centre of mass averaged position of the entire glycan (without the C5 tail) called $\vec{G}$. We can now calculate the distance d of the glycan towards the coiled-coil with:

$$d = \frac{|\vec{G} \times \vec{v}|}{|\vec{v}|}$$

(12)

For the position along the coiled-coil we use the relative position r since the length slightly varies by simulation frame and it is easier to see the length of the original coiled-coil. Due to the linker and the C5 chain, the glycan can extend beyond the coiled-coil in both directions. 0% and 100% are the N- and C-Terminus respectively (without the chromophore). The relative position can be calculated with:

$$r = \frac{\vec{G} \cdot |\vec{v}|}{|\vec{v}|} \, 100\%$$

(13)

Cryo-transmission electron microscopy

Cryo-transmission electron microscopy (cryo-TEM) was measured of 0.1% (w/v) peptide hydrogel samples that were prepared as described above. Peptide gel aliquots of 5 µL were applied on pre-cleaned 200 mesh perforated carbon film-covered microscopical grids (R1/4 batch of Quantifoil, MicroTools GmbH, Jena, Germany). The grids were cleaned with chloroform and hydrophilized by 60 seconds glow discharging at 8 W in a BALTEC MED 020 device (Leica Microsystems, Wetzlar, Germany). The samples were blotted and vitrified using a FEI Vitrobot Mark IV and liquid ethane as cryogen. After transferral to a FEI TALOS ARCTICA electron microscope equipped a with high-brightness field-emission gun (XFEG) operating at an acceleration voltage of 200 kV, micrographs were acquired on a FEI Falcon 3 direct electron detector (Thermo Fisher Scientific Inc., Waltham, Massachusetts, USA) using a 70 µm objective aperture at a nominal magnification of 28000 or 36000, corresponding to a calibrated pixel size of 3.69 or 2.97 Å/pixel, respectively.

Results and Discussion

Synthesis

Peptides were synthesised using Fmoc-SPPS and remained attached to the solid support. Glycans were synthesised according to literature reports[24-28] and coupled to the peptide on the solid phase. After cleavage from the solid support and HPLC purification, the anions were exchanged from trifluoroacetic acid to chloride.

Structural analysis

All glycopeptides were studied at different concentrations by means of circular dichroism (CD) spectroscopy. CD spectra at 0.1% (w/v) exhibit characteristic signals for α-helical structures, namely an ellipticity maximum at 195 nm and two minima, at 208 nm and 222 nm (Figure 2a).

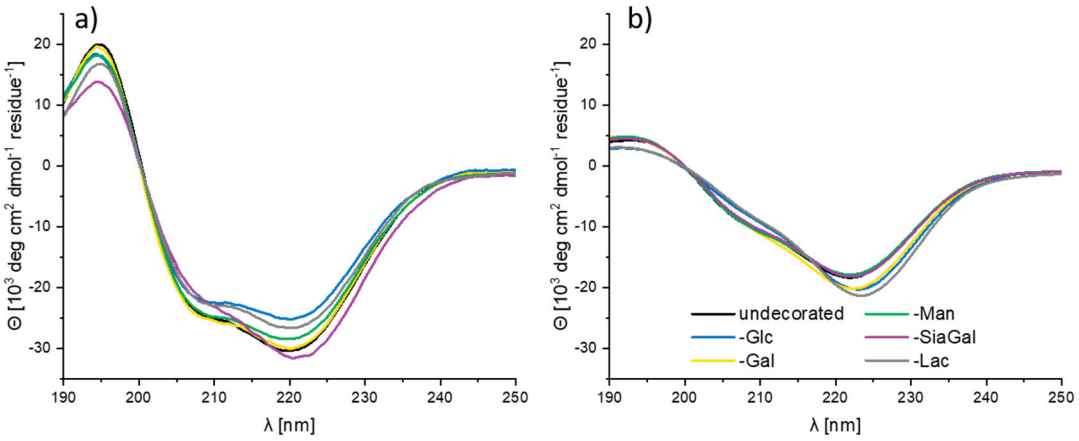

Figure 2: CD spectra of glycan-decorated peptides at 0.1% (w/v) (a) and 0.5% (w/v) (b) in DPBS recorded at pH 4 and 37 °C.

At 0.5% (w/v) (Figure 2b), the maximum attenuates while the average intensity ratio of the two minima ($\theta_{222\ nm}/\theta_{208\ nm}$) shifts from 1.22 ± 0.11 towards 2.21 ± 0.35. This behaviour has been attributed to the formation of higher order helical structures[41] and is also in accordance with structural findings on the parent system hFF03[14]. Variations between the differently decorated peptides are minimal. It seems that α-helix and fibre formation occur regardless of the introduced glycan. This is line with the finding that the assembly occurs via a contact between C-terminus and N-terminus of the coiled-coils.[22]

Furthermore, the secondary structure of 0.5% (w/v) undecorated backbone hFF03 was evaluated at different pH values. As can be seen from Figure 3, the CD spectra are very similar, suggesting that the secondary structure is not perturbed by changes in pH. While the curve intensity is less pronounced at pH extremes (3.4 and 11.4) the curve shape remains unchanged meaning that the coiled-coils still assemble. From the generally higher intensity as compared to buffered conditions (Figure 2b) it can be concluded that helicity is stronger in unbuffered conditions.

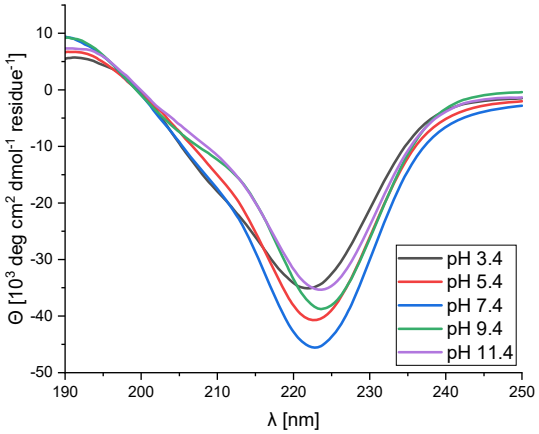

Figure 3: CD spectra of 0.5% (w/v) hFF03 at different pH values, recorded at 37°C. Samples were prepared in water + 150 mM NaCl and pH adjusted using 1 M NaOH and HCl.

Overall, CD experiments show that the hFF03-based coiled-coil motif is robust to incorporation of single glycans and change of pH. At higher concentration, CD indicates the formation of superstructures.

Cryo transmission electron microscopy (cryo TEM)

The morphology of the decorated peptides was investigated by cryo TEM. Solutions of 0.5% (w/v) of hFF03-Man and hFF03-SiaGal were prepared as described above and then diluted to 0.05% (w/v) using DPBS since fibre density was too high to obtain meaningful micrographs otherwise. As can be seen from Figure 4, both hydrogels exhibit a network of extended fibres of about 3 nm diameter.

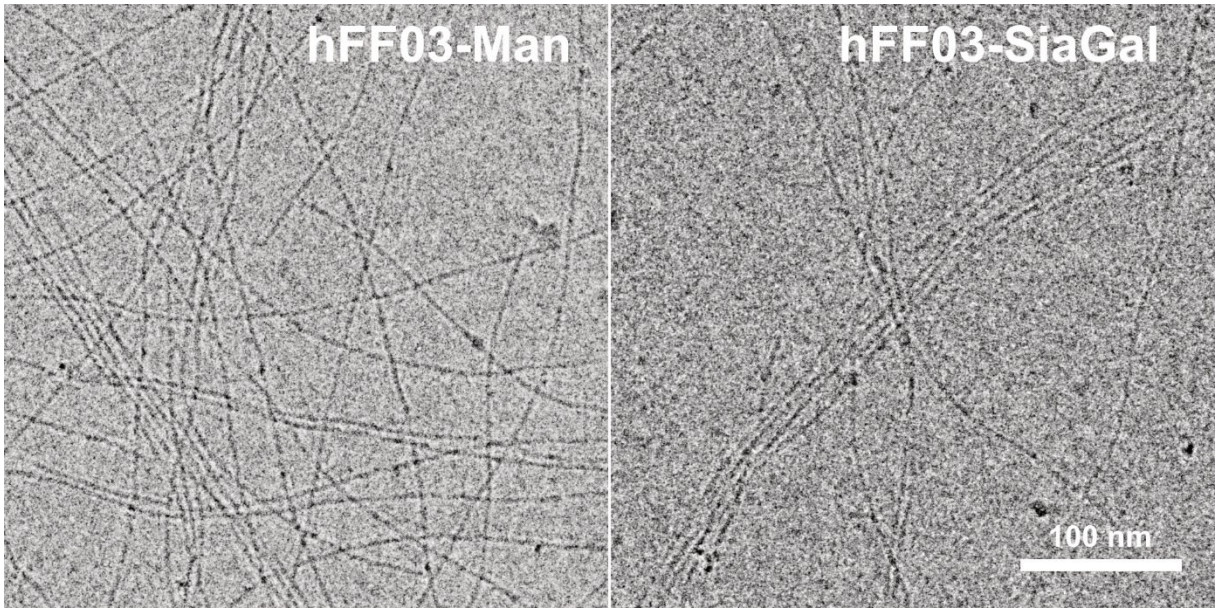

Figure 4: Cryo transmission electron microscopy (cryo TEM) images of 0.05% (w/v) peptide hydrogels, Man-decorated (left) and SiaGal-decorated (right). The scale bar denotes 100 nm.

This morphology is also described for the undecorated parent peptide hFF03[14] and we therefore conclude that fibre formation is not altered by glycan decoration.

Simulations (MD)

We conducted MD simulations of α-mannose-hFF03, β-galactose-hFF03 and β-glucose-hFF03 in explicit water to examine the structure and dynamics of the glycosylated linker. The glycans are connected through an extended linker to lysine at position 18, i.e. towards the C-terminus of the coiled-coil. Due to the length of the linker, the glycan can reach up to 4 nm into the solvent (Figure 5 A-C). Although this extension is significant, especially when considering that the coiled-coil's length is 4 nm, it is not enough to span the mesh sizes which are around 50 nm in the undecorated hFF03[22] and up to around 80 nm in the glycosylated hFF03 (Table 1) as determined from macrorheology. The glycosylated linker in β-galactose-hFF03 (Figure 5 B) extends slightly further and more frequently into the solvent than in the other two simulated systems.

Overall, however, the extended conformation of the linker is a minor conformation. In the vast majority of the linker conformations, the glycans form interactions with the coiled-coil peptide. For example, they intercalate between two lysine side chains (Figure 5 E). This conformation is characterized by a relative position of 50-75% along the coiled-coil axis and a distance of around 1 nm from the axis and is particularly frequently populated in β-glucose-hFF03 (Figure 5 C).

The linker can also extend up to the C-terminus of the coiled-coil peptide, where the glycan forms a stable interaction with the terminal residues. This conformation is characterized by a relative position of 100% along the

coiled-coil axis and a distance less than 1 nm from the axis. This conformation likely competes with the self-assembly of the coiled-coils into fibrils, which are stabilised by a salt-bridge network between the C-terminus and the N-terminus of consecutive coiled-coils[22]. Thus, structure and dynamics of the linker may interfere with the hydrogelation process, and shortening the linker might stabilise the hydrogels.

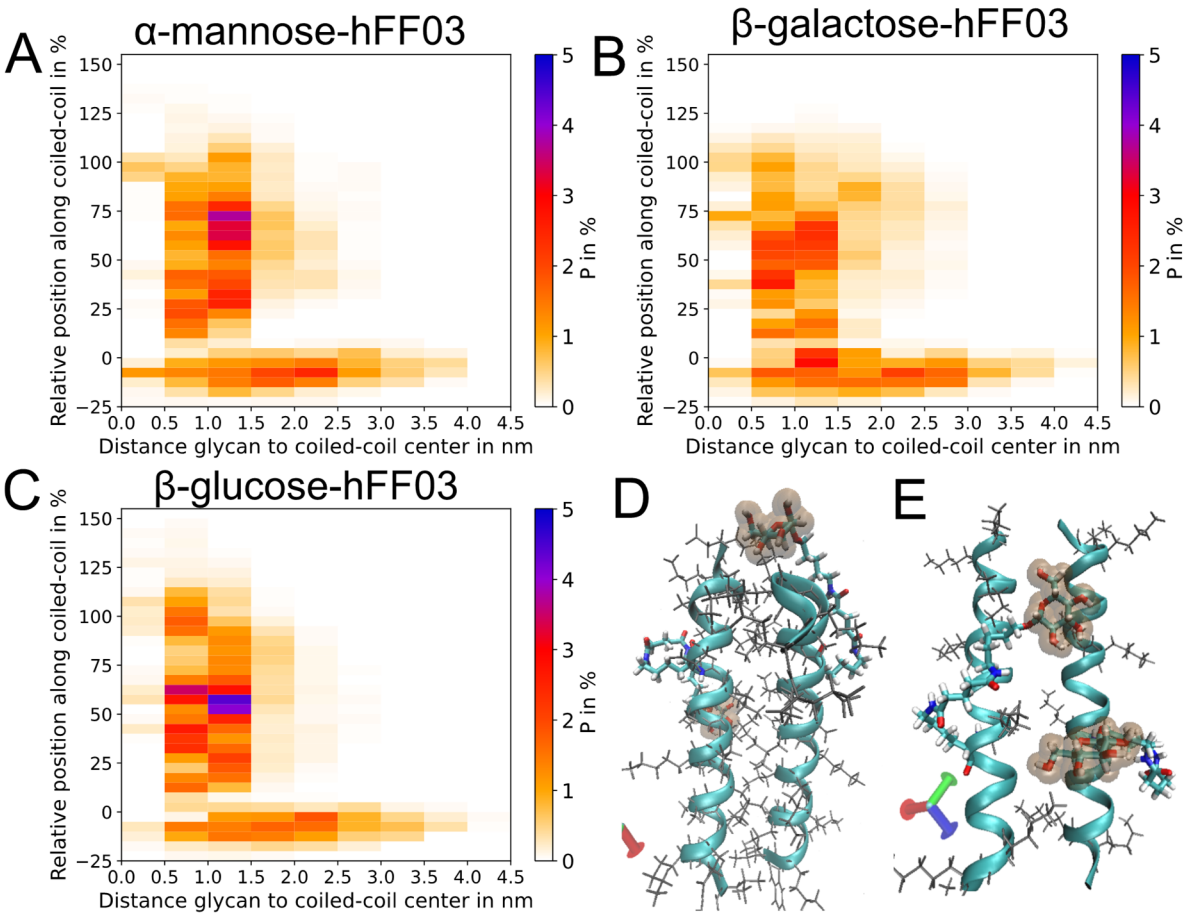

Figure 5: A-C: 2D histogram of the relative positions of the glycan towards its coiled-coil with α-mannose-hFF03 (A), β-galactose-hFF03 (B) and β-glucose-hFF03 (C). The colour denotes the occurrence rate over all coiled-coils and simulation time. D and E show a single coiled-coil with the glycan highlighted to demonstrate the common configurations. D: the glycan is on top of the C-terminus. E: the glycan is nestled between two lysine sidechains.

Viscoelastic properties

Macrorheology

The rheological properties of 0.5% (w/v) solutions of peptide, decorated with various glycans, were studied by means of oscillatory shear rheology. In oscillatory shear rheology, samples are subjected to an oscillating shear strain which yield the storage modulus G' (elastic response) and the loss modulus G'' (viscous response) as a function of frequency. The frequency sweep results are shown in Figure 6.

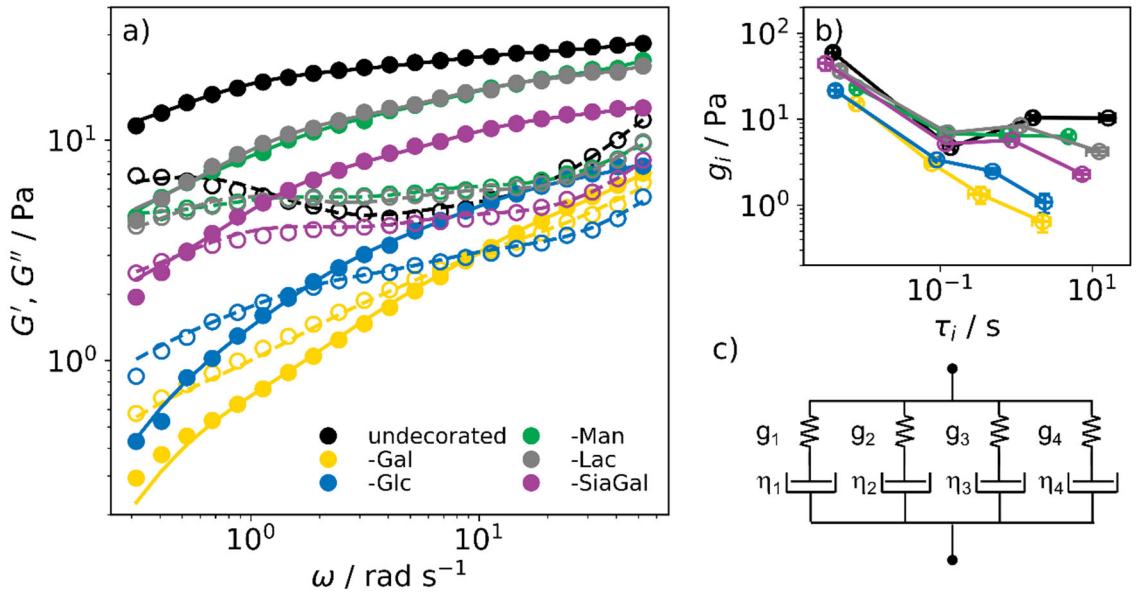

Figure 6: a) Frequency sweep data (filled symbols: G', open symbols: G'') and generalized Maxwell model (GMM) fits (solid lines: G', broken lines: G'') for solutions of the undecorated and decorated peptides (concentration always 0.5% w/v in DPBS at pH 4). b) Relaxation times and strengths as determined from GMM fits. c) Graphical representation of the generalized Maxwell model with 4 Maxwell elements connected in parallel. Experimental conditions: 37 °C.

All peptide solutions show viscoelastic properties with values for G' and G'' ranging from around 0.1 to 30 Pa. For all glycan-decorated peptides, a decrease in the viscoelastic response is observed compared to the undecorated peptide. The undecorated peptide shows the strongest viscoelastic response and has typical gel-like behaviour, since $G' > G''$ over the whole frequency range and both moduli vary only slightly with frequency.[42] The solutions of the Man-, Lac- and SiaGal-decorated peptides can still be considered soft hydrogels since G' dominates over most of the frequency range.

To obtain further insight, the frequency sweep data were fitted with the generalized Maxwell model (GMM), also referred to as the Wiechert model.[43-45] This model is based on the idea that the overall viscoelastic relaxation is given by a superposition of individual exponential relaxation processes. It is made up of N Maxwell elements, that are arranged in parallel. For the frequency dependence of G' and G'' we find

$$G'(\omega) = \sum_{i=0}^{N} g_i \frac{\tau_i^2 \omega^2}{1 + \tau_i^2 \omega^2} \quad (14)$$

$$G''(\omega) = \sum_{i=0}^{N} g_i \frac{\tau_i \omega}{1 + \tau_i \omega^2} \quad (15)$$

where τ_i and g_i are the relaxation time and relaxation strength of the i-th mode. To avoid overfitting and to achieve comparability between the fit results, we fix the number of modes to 4. The fits of G' and G'' are shown as full and broken lines, respectively, in Figure 6a and the determined relaxation times and strengths in Figure 6b. The behaviour at high frequencies corresponds to processes taking place in a short time and vice versa. Looking at the relaxation time spectra in Figure 6b, it is clear that the slower dynamics are much more affected than the faster

dynamics. A stronger gel character, such as in the undecorated and Man-, Lac- as well as SiaGal-decorated peptide samples is clearly associated with an increase of the relaxation strength of the slowest two relaxation modes and an increase of the relaxation times. This indicates the presence of a slower dynamical process taking place in the case of the gel samples, most likely on a larger length scale. The faster dynamical processes taking place on a more local scale remain largely unaffected.

When studying hydrogels, one important quantity to be discussed is the mesh size ξ, which is the average distance between crosslinking points in a network structure.[46] While this quantity is not accessible experimentally, we can estimate it from the plateau modulus G_0, which is the value of G' at the high frequency plateau. According to classical rubber elasticity theory[47-49], the plateau modulus G_0 can be related to the number density of effective crosslinking points and therefore to a corresponding mesh size ξ (sometimes also referred to as the elastic blob[46]) in a hydrogel by

$$G_0 = \frac{kT}{\xi^3} \qquad (16)$$

where k is the Boltzmann constant and T is the temperature in K. For our case, we take the plateau modulus to be equal to the value of the storage modulus at the highest measured frequency $G_0 = G'(\omega = 52.4$ rad/s). For some samples, a slope is observed at this frequency instead of a true plateau, so the determined values of G_0 and the derived ξ only serve as rough estimates. In general, a larger plateau modulus is associated with a smaller mesh size. Accordingly, we find that the mesh size is smallest for the undecorated peptide at 53.1 nm and increases to up to 83.4 nm for the galactose-decorated peptide. All mesh sizes are shown in Table 1.

Table 1: Results for the mesh size ξ of different 0.5% (w/v) peptide hydrogels at pH 4 and 37 °C, determined from the value of G' at $\omega = 52.4$ rad/s.

Sample	**G_0 / Pa**	**ξ / nm**
Undecorated	27.5	53.1
-Gal	7.1	83.4
-Glc	7.6	81.4
-Man	23.0	56.4
-Lac	21.7	57.5
-SiaGal	14.0	66.5

Additionally, continuous shear experiments were performed. The shear rate was first increased from 0.01 to 100 1/s (up-sweep) and then decreased (down-sweep) to check for hysteresis effects. The results are shown in Figure 5.

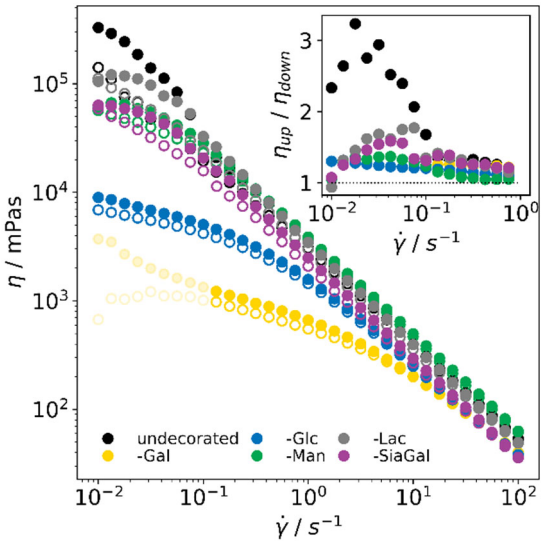

Figure 7: Results of continuous shear experiments performed on 0.5% (w/v) peptide hydrogels at pH 4 and 37°C. The up- and down-sweep data points are shown with filled and open circles, respectively. Since significant effects of hysteresis were detected, the ratios between the up- and down sweeps are shown in the inset. For the very low viscous galactose-decorated samples, an unrealistic decrease of the viscosity was detected in the down sweep at low shear rates. In this case, only the data points above 0.1 s^{-1} were considered for the inset. The remaining data points are shown in a lower saturated yellow.

All samples show shear-thinning behaviour. The undecorated peptide, as well as the Lac- and SiaGal-decorated peptides show a significantly higher viscosity at low shear rates than the Gal- and Glc-decorated variants. In addition, there are hysteresis effects, which are quantified by the ratios between the up- and down-sweep data sets, which are shown in the inset in Figure 7. In the case of the undecorated sample, the viscosity determined in the up-sweep at low shear rates is up to 3 times larger than in the down-sweep. The largest differences are seen for shear rates below 0.1 s^{-1}. The presence of hysteresis could indicate the existence of a (self-assembled) superstructure that is destroyed upon strong shearing and not fully reformed within the time frame of the experiment, which in our case was between 4.6 min for the SiaGal- and 20.9 min for undecorated sample (see experimental section for details). In any case, the presence of the hysteresis effects demonstrates that self-healing of the hydrogel structure in these systems requires substantial time and this effect is more strongly observed for the undecorated sample.

To check for the influence of pH, macrorheology was performed on the undecorated hFF03 peptide at different pH values between 3.4 and 11.4. As can be seen from Figure 8, at all probed pH values, except for pH 11.4, the peptide shows typical gel behaviour, with *G*' dominating *G*'' over the whole frequency range and the moduli being virtually independent of frequency.[42] At pH 11.4 the sample behaves liquid-like since *G*' < *G*''. It is safe to assume that at this point the electrostatic interactions between N- and C-termini collapse because the N-terminal amino group of *ortho*-aminobenzoic acid (pK_a ~ 11.8[50]) is no longer protonated and therefore uncharged. Approaching pH 10 the sample briefly became turbid indicating limited peptide solubility at the isoelectric point (pI ~ 10.3), before turning clear again at pH > 11.

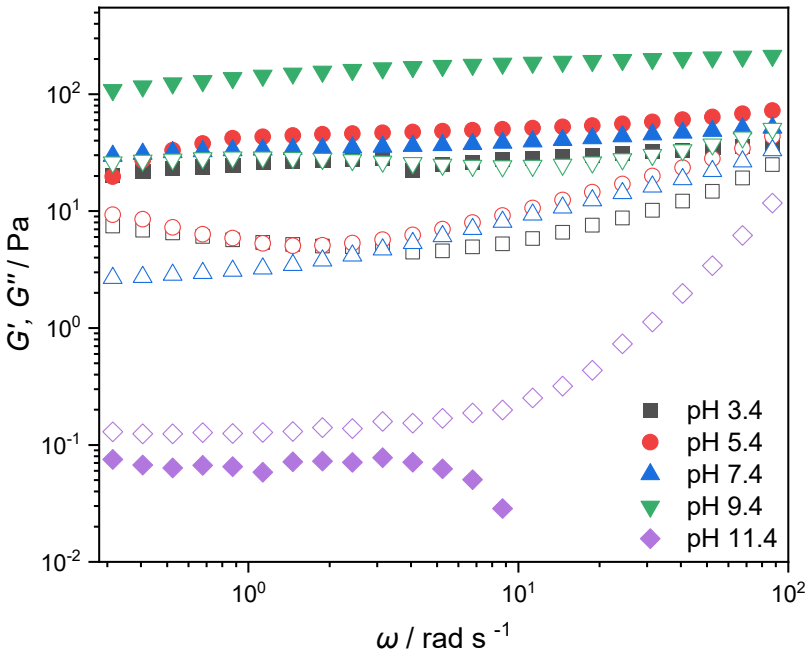

Figure 8: Frequency sweep data (filled symbols: G', open symbols: G'') of 0.5% (w/v) hFF03 at different pH. Samples were prepared in water + 150 mM NaCl and pH adjusted using 1 M NaOH and HCl, measured at 37 °C.

When comparing the effective rheological mesh sizes (Table 2), it can be seen that at the values at pH 3.4, 5.4 and 7.4 are largely similar (40.-49.7 nm), while at pH 9.4 a smaller mesh size of 27.5 nm is found. This corresponds to the highest measured elastic response, making it the "stiffest" of all investigated hydrogels.

Table 2: Results for the mesh size ξ, determined from the value of G' at ω = 52.4 rad/s of 0.5% (w/v) undecorated hFF03 peptide at different pH and 37 °C.

Sample	**G_0 / Pa**	**ξ / nm**
pH 3.4	34.9	49.7
pH 5.4	63.9	40.6
pH 7.4	48.5	44.5
pH 9.4	207.1	27.5
pH 11.4	no hydrogel	

Overall, the pH-dependent experiments showed that the peptide backbone robustly forms hydrogels across a large and mucus-relevant pH-range.[51]

To investigate the influence of pH value on glycan-decorated peptides macrorheology was carried out at pH 7.4. The frequency sweep data is shown in Figure 9. The overall curve shape for the elastic response is very similar to pH 4. The storage modulus G' is larger than the loss modulus G'' for all hydrogels. In contrast to the behaviour at pH 4 (Figure 6a), the influence of glycan decoration seems to follow a different pattern here. While the samples

decorated with monosaccharides (Glc, Gal, Man) show very similar behaviour among each other, their viscoelastic response being higher than the undecorated peptide, the viscoelastic response of the disaccharide-decorated SiaGal-peptide is weaker as compared to the undecorated peptide.

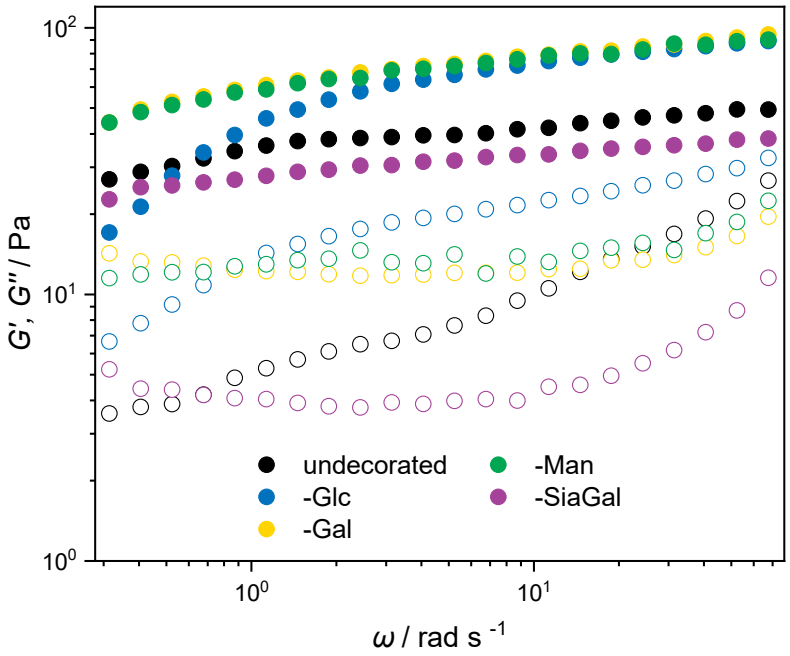

Figure 9: Frequency sweep data (filled symbols: G', open symbols: G'') for undecorated and decorated peptides at pH 7.4. Samples were prepared at 0.5 % (w/v) in DPBS, pH adjusted to 7.4 using 1 M NaOH and measured at 37 °C.

Comparing the plateau modulus G_0 and the derived mesh size ξ at pH 4 (Table 1) and pH 7.4 (Table 3), all hydrogels are stiffer at pH 7.4, as shown by an increase in G_0 (and corresponding decrease in mesh size). However, this increase is of different magnitude depending on the decoration. While the monosaccharide-decorated peptides show the largest increase (more than 10-fold for Gal and Glc, more than 4-fold for Man), it is less pronounced for the disaccharide-decorated SiaGal-peptide (2.7-fold) and least for the undecorated peptide (1.6-fold). Overall, this leads to a different trend at pH 7.4. The "stiffest" hydrogels are the monosaccharide-decorated ones, followed by the undecorated and the disaccharide-decorated peptide hydrogel.

Table 3: Results for the mesh size ξ of different 0.5% (w/v) peptide hydrogels at pH 7.4, determined from the value of G' at ω = 52.4 rad/s.

Sample	**G_0 / Pa**	**ξ / nm**
Undecorated	49.4	44.3
-Gal	91.9	36.0
-Glc	87.6	36.6
-Man	89.1	36.4
-SiaGal	38.0	48.3

In summary, from the macrorheology experiments it is clear that the choice of glycan has a measurable effect on the viscoelastic properties of the peptide hydrogels. However, this effect varies between different pH values and when it comes to magnitude, pH-effects can exceed glycan-effects. pH-dependant viscoelastic properties are also found for many native or reconstituted mucus hydrogels.[51,52] Analysis with the generalized Maxwell model shows that samples with gel-character exhibit a slower dynamical process. They also exhibit mucus-like shear-thinning behaviour[52] and hysteresis in steady shear experiments, indicative of a self-assembled superstructure.

Microrheology

For dynamic light scattering (DLS) microrheology tracer particles were added to the samples in the gel formation process. By scattering measurements, their mean squared displacement (MSD) and subsequently storage (G') and loss modulus (G'') can be determined. The MSD of the peptide hydrogels are shown in Figure 10a. Note that for the -Lac sample, only one measurement was performed instead of three, due to limited sample availability.

At very short lag times ($\tau < 10^{-4}$ s) the MSD is proportional to τ, indicating diffusive motion, characterized by the zero-shear viscosities of the solvent.[53] At intermediate lag times ($\tau > 10^{-4}$ s), the tracer particles undergo subdiffusive motion, i.e., MSD $\sim \tau^{\alpha}$, where $0 < \alpha < 1$. The time dependence of $\alpha(\omega = \tau^{-1})$ contains information about the viscoelastic properties of the sample. For the diffusive region at short lag times, we perform linear fits of the first 10 data points and obtain the associated diffusion coefficients, since $\langle \Delta r^2 \rangle = 6D\tau$ for diffusive motion in 3D. From the diffusion coefficients, we can calculate the viscosity using the Stokes-Einstein equation

$$\eta = \frac{kT}{6\pi RD} \tag{17}$$

where R = 96.0 nm is the tracer particle radius.

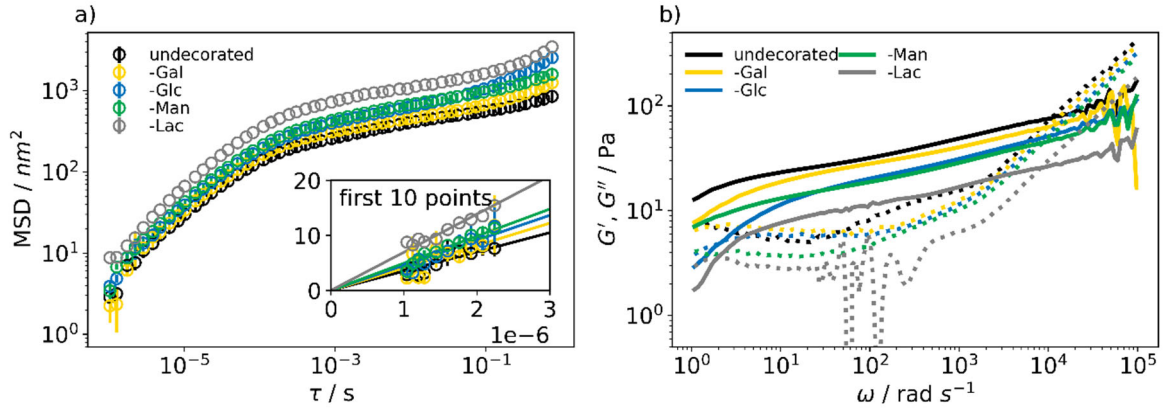

Figure 10: a) MSDs of peptide hydrogels as determined by DLS measurements. The point density was decreased for better lucidity. The insets show linear fits to the first 10 data points, which yield the zero-shear viscosity of the solvent. b) Results for

G' (full lines) and *G*'' (dotted lines) from DLS microrheology. Experimental conditions: 0.5% (w/v) peptide in DPBS at pH 4, 25°C.

The diffusion coefficients, viscosities and mesh sizes are summarized in Table 4. When looking at the mesh sizes obtained from microrheology, they all lie between 53.0 and 74.0 nm, which is consistent with the values obtained from macrorheology (53.1-81.4 nm, Table 1). However, again different trends can be found.

Table 4: Diffusion coefficient and viscosity as determined from linear fitting of the short and long lag time behaviour of the MSD. Results for the mesh size ξ of 0.5% (w/v) peptide hydrogels at pH 4, determined from the value of *G*' at ω = 52.4 rad/s.

Sample	***D* / nm^2 s^{-1}**	**η / mPas**	**G_0 / Pa**	**ξ / nm**
Undecorated	(5.83 ± 0.30) x 10^5	3.45 ± 0.18	28.8	53.0
-Gal	(6.78 ± 0.64) x 10^5	2.97 ± 0.28	25.6	55.1
-Glc	(7.58 ± 0.33) x 10^5	2.66 ± 0.12	18.0	62.0
-Man	(8.21 ± 0.23) x 10^5	2.45 ± 0.07	17.1	63.0
-Lac	(1.15 ± 0.03) x 10^6	1.74 ± 0.04	10.6	74.0

The determined solvent viscosities are significantly larger than that of DPBS buffer (0.9041 mPas), indicating that the local movement of the tracer particles is sensitive to the presence of the peptide-glycan chains. Overall, we have demonstrated that DLS microrheology is a viable technique to determine the viscoelastic properties of peptide hydrogels over a wide frequency range, reducing the necessary sample volume to around ~50 µL. There is generally good agreement between macro- and microrheology, although the precise values for G_0 are slightly different between the two techniques. The local solvent viscosity around the tracer particles is significantly larger than that of the pure solvent.

Nanorheology

Cy3 viscosity calibration and hFF03 hydrogel formation kinetics.

Cyanine 3 (Cy3) belongs to the class of so-called fluorescent molecular rotors (FMRs) that have emerged as novel nanoprobes for dynamic and spatially resolved nanoviscosity sensing.[30] We recently established a Cy3 dye as a fluorescent molecular rotor for membrane nanoviscosity measurements and extensively characterized the fluorescence characteristics of Cy3 as a function of temperature and viscosity.[30] Nanoviscosity is the apparent viscosity sensed by a small molecular probe on the nanoscale in complex liquids/gels [54,55]. The excited state lifetime of Cy3 (ICC) in aqueous solution is very short (τ~0.14-0.18 ns[56-58]) due to a highly efficient rotation (twisting motion) around the C-C bond of the ICC methine-linker [59]. When bond rotation is hindered, either by friction with solvent molecules (viscosity) or by steric hindering, e.g., through binding to biomolecules, the radiative pathway becomes populated generating fluorescence[58,60-62].

Here, we use the fluorescent molecular rotor (FMR) dye Cy3 as a nanoviscosity probe to directly measure the viscosity within a 0.5% (w/v) hFF03 peptide hydrogel at pH 4 and 25 °C (Figure 11). A calibration curve connects the mean fluorescence lifetime of Cy3 (τ_{mean}) to the known bulk viscosity of a buffer/sucrose mixture (Figure 11a).

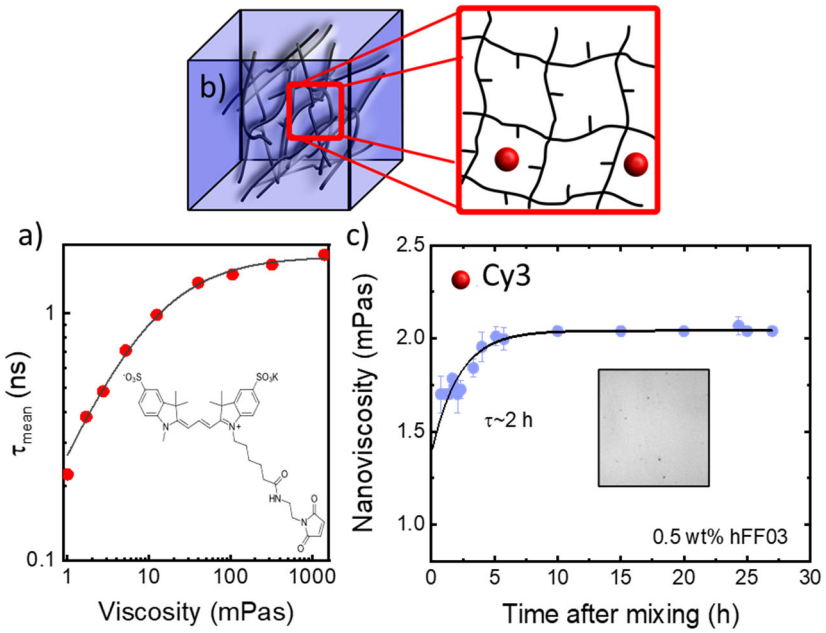

Figure 11: (a) Viscosity calibration curve fitted with a modified Förster-Hoffmann equation (Eq. 15). The chemical structure of Cy3 (sulphated cyanine 3 maleimide) is shown in the inset. b) Schematic of nanoviscosity measurement design using Cy3. c) Changes of nanoviscosity as a function of gel formation time and a monoexponential fit to the data. The time constant τ for gel formation is indicated. An initial viscosity of the aqueous hFF03 mixture at t=0 is extrapolated from the fit with 1.138 mPas. The inset shows the image from the FLIM measurement indicative of homogeneous Cy3 nanoviscosity sensor distribution. Experimental conditions: 0.5 µM Cy3 in DPBS/sucrose mixtures, respectively, in 0.5% (w/v) hFF03, 25 °C.

Using this viscosity calibration curve, we analysed the nanoviscosity of hFF03 at different time points in a 24 h time window after adding DPBS to the hFF03 peptide. Three gelation experiments were performed yielding a mean nanoviscosity value of 2.0 ± 0.3 mPas for 0.5% (w/v) hFF03 at 25 °C, to which the various experiments were normalised. A fit of the kinetics with an exponential function result in a time constant of ~ 2 h for gel formation based on the temporal development of the nanoviscosity, indicating that the gel formation process is safely completed after 10 h (Figure 11c). For all rheology experiments, the samples were incubated for 16-24 h before measurement.

Nanoviscosity of glycan-decorated hFF03

Next, we evaluated the Cy3 fluorescence decay curves in the different glycan-decorated hFF03 peptide hydrogels at 0.5% (w/v) and pH 4 as shown in Figure 12a. The mean lifetimes and corresponding viscosity values are shown in Figure 12b and c. All nanoviscosity values range between 2 and 3 mPas (Table 5), clearly above the value for pure buffer (0.904 mPas).

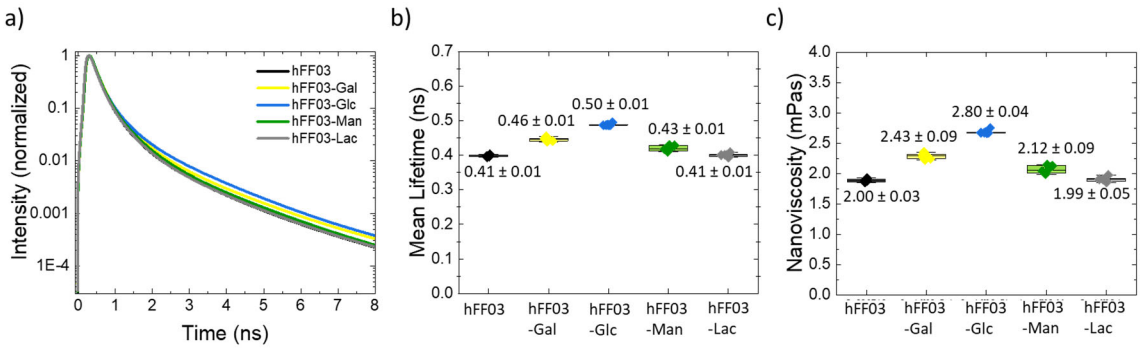

Figure 12: Nanoviscosity of glycan-decorated hFF03 peptide hydrogels. a) Cy3 fluorescence decay curves in the different peptide hydrogels. b) Mean fluorescence lifetimes. c) Nanoviscosity of the sugar-decorated peptides with galactose (Gal), glucose (Glu), mannose (Man), and lactose (Lac). hFF03 is shown for comparison. Experimental conditions: 0.5 µM Cy3 in 0.5% (w/v) hFF03, 25°C. For each nanoviscosity value 4-6 measurements were performed and analysed.

Overall, they are very similar to the solution viscosity data determined using DLS (Table 4 right column) with values between 1.7 and 3.5 mPas. However, different trends are found. While the most viscous gel as per DLS was formed by the undecorated hFF03 peptide, here it seemed to be the glucose-decorated sample, followed by galactose and mannose. This seems to reflect the order found by macrorheology at pH 7.4 (Table 3). A possible explanation is that the determination of nanoviscosity is more susceptible to slight variations in peptide concentration, pH value or salt content which might lead to significant deviations here, possibly exceeding the glycan influence.

Table 5: Nanoviscosities of undecorated and glycan-decorated hFF03 at 0.5% (w/v), pH 4 and 25°C as determined from fluorescence lifetime spectroscopy using the Cy3 viscosity calibration and the modified Förster-Hoffmann equation.

Sample	***η*** **(mPas)**
Undecorated	2.00 ± 0.03
-Gal	2.49 ± 0.09
-Glc	2.80 ± 0.04
-Man	2.12 ± 0.09
-Lac	1.99 ± 0.05

From Nano- to Micro- to Macrorheology.

For two selected samples, undecorated hFF03 and hFF03-Man, a direct comparison was made for the nano, micro, and macrorheology measurements. Measurements were performed on aliquots of the same sample (0.5% (w/v), pH 4, 25 °C) on the same day using Cy3 time-resolved fluorescence nanorheology, DLS microrheology, and macrorheology.

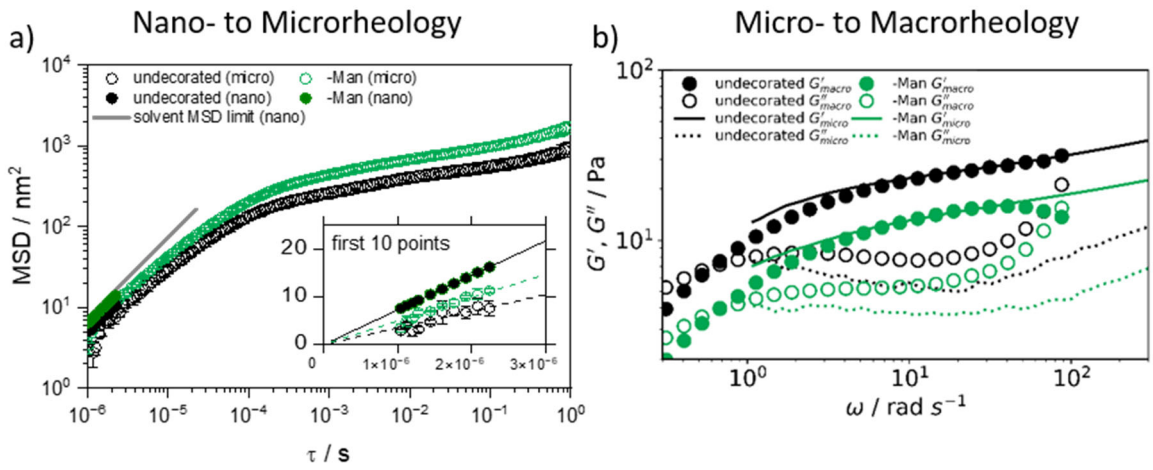

Figure 13: Direct comparison of nano, micro, macroviscosity data of two selected samples from which aliquots were measured at the same day with Cy3 fluorescence, DLS, and macrorheology, respectively. The comparison between MSDs calculated from the Cy3 time-resolved fluorescence (nanoviscosity) and from DLS measurements (microrheology) is shown in a). The comparison between the same DLS data and macrorheology experiments is shown in b), where G' and G'' are given by the filled and open symbols respectively. Experimental conditions: 0.5% (w/v), pH 4, 25 °C.

In Figure 13a the MSD traces from nanoviscosity and microviscosity experiments are compared. A direct comparison between data obtained from the Cy3 fluorescence and DLS measurements is possible at very short times, for which MSD ~ τ, thus indicating a diffusive motion in the solvent. The solvent viscosity values resulting from the nanoviscosity measurements are lower than those obtained from DLS, as illustrated by the steeper slope of the MSD plot (Figure 13a). The inset shows a zoom of this time window with a linear fit for the first 10 data points of the DLS measurements, yielding the solvent viscosity for the undecorated peptide with 3.45 ± 0.18 mPas, and for the mannose-decorated peptide with 2.45 ± 0.07 mPas. The corresponding value obtained from nanoviscosity is 1.80 ± 0.05 mPas, for both undecorated and Man-peptide.

We interpret the values such that the nanoviscosity gives the bulk solvent viscosity, while the DLS analysis yields the viscosity of an interfacial layer of solvent around the particle, which would be slightly increased in comparison to the bulk. Netz *et al.* found evidence for the formation of an interfacial water layer with an increased water viscosity using nonequilibrium molecular dynamics simulations.[63] We are currently investigating the applicability of this concept to tracer particles in DLS microrheology as well as a combination of tracer particle-based MSD and tracer-bound FMR-based nanoviscosity determination.

For the comparison between micro- and macrorheology, the results are shown in Figure 13b using symbols. In general, there is good agreement between the two methods in the overlapping frequency range for the storage modulus G'. The loss modulus G'' determined by microrheology tends to be somewhat smaller than determined by macrorheology. The frequency dependence of G' and G'' in the high frequency regime is markedly different. G' shows a slow increase with a rather constant power law exponent of around 0.17. For frequencies below 10^3 rad/s G'' is smaller than G' and decreases only slowly but shows a strong increase at high frequencies.

Overall, the comparison of three rheology techniques shows that, although they focus on very different length scales, they can be combined to give a complete and consistent picture of the described hydrogels.

Conclusion

In this study we presented a simple peptide-based model for some key properties of mucus, i.e., viscoelastic behaviour and the presentation of defined carbohydrate moieties. We used three complementary rheology techniques to gain an understanding of the hydrogels across all relevant length scales.

On the one hand, we found the hydrogel structure was profoundly robust towards glycan-decoration. The secondary structure was not perturbed by introduction of glycans as shown by CD spectroscopy. Cryo-TEM showed that fibre morphology was the same for Man- and SiaGal-decorated gels, as well as comparable to undecorated peptide. All samples that were investigated at physiologic pH formed self-supporting hydrogels with elastic moduli in the range between 38 and 90 Pa.

On the other hand, we found differences in the viscoelastic behaviour depending on glycan decoration and pH value. This behaviour cannot be rationalised solely by the structural findings. Therefore, we think that the differences must be based on dynamic processes. CD spectroscopy does not show this behaviour because spectra are accumulated over several minutes and therefore only depict an ensemble average. The arrested cryo-state cannot reflect this behaviour either. However, MD simulations of the undecorated hFF03 show that fibrils are highly dynamic and rearrange on the nanosecond timescale. Oligomers and eventually fibrils are formed via a salt-bridge network between the C- and the N-terminus of consecutive coiled-coils. The oligomers can rearrange by forming Y-junctions from which a short segment can dissociate.[22] The differently decorated peptides might differ in the speed of rearrangement and the efficiency in which the fibril network accommodates the shear strain. Specifically, due to the long and flexible linker, the glycan can form an interaction with the C-terminus of its coiled-coil peptide, thereby competing with the self-assembly of two coiled-coils dimers into an oligomer. Thus, rheological data shows more variety between different glycans than the more "static" methods such as CD and cryo-TEM.

The advantage of this peptide hydrogel clearly lies in its versatility. While it is difficult to quantify the influence of one glycan across different pH and methods, it is clear that viscoelastic properties can be tuned to match desired mucus properties. Therefore, this peptide hydrogel could be used to study more applied questions such as pathogen interaction with mucus-derived glycans within a hydrogel context. To bring the model system closer to the very intricate native mucus it would be interesting to gradually increase the complexity of the system, for example by adding more copies of complex glycans.

Acknowledgements

The authors gratefully acknowledge funding by the Deutsche Forschungsgemeinschaft (DFG) through the collaborative research centre 1449 "Dynamic Hydrogels at Biointerfaces" (Project ID 431232613) and the core facility BioSupraMol. Furthermore, the authors would like to thank the HPC Service of ZEDAT, Freie Universität Berlin, for computing time.[39] MD and MCSDC thank the Max Planck Society for financial support.

Conflict of interest

There are no conflicts to declare.

References

1 Wagner, C. E., Wheeler, K. M. & Ribbeck, K. Mucins and Their Role in Shaping the Functions of Mucus Barriers. *Annual Review of Cell and Developmental Biology* **34**, 189-215, doi:10.1146/annurev-cellbio-100617-062818 (2018).

2 Wang, B. X., Wu, C. M. & Ribbeck, K. Home, sweet home: how mucus accommodates our microbiota. *The FEBS Journal* **288**, 1789-1799, doi:https://doi.org/10.1111/febs.15504 (2021).

3 Bansil, R. & Turner, B. S. Mucin structure, aggregation, physiological functions and biomedical applications. *Current Opinion in Colloid & Interface Science* **11**, 164-170, doi:https://doi.org/10.1016/j.cocis.2005.11.001 (2006).

4 Leal, J., Smyth, H. D. C. & Ghosh, D. Physicochemical properties of mucus and their impact on transmucosal drug delivery. *International Journal of Pharmaceutics* **532**, 555-572, doi:https://doi.org/10.1016/j.ijpharm.2017.09.018 (2017).

5 Wang, B. X. *et al.* Host-derived O-glycans inhibit toxigenic conversion by a virulence-encoding phage in Vibrio cholerae. *The EMBO Journal* **42**, e111562, doi:https://doi.org/10.15252/embj.2022111562 (2023).

6 Bej, R. & Haag, R. Mucus-Inspired Dynamic Hydrogels: Synthesis and Future Perspectives. *Journal of the American Chemical Society* **144**, 20137-20152, doi:10.1021/jacs.1c13547 (2022).

7 Lai, S. K., Wang, Y.-Y., Wirtz, D. & Hanes, J. Micro- and macrorheology of mucus. *Advanced Drug Delivery Reviews* **61**, 86-100, doi:https://doi.org/10.1016/j.addr.2008.09.012 (2009).

8 Kočevar-Nared, J., Kristl, J. & Šmid-Korbar, J. Comparative rheological investigation of crude gastric mucin and natural gastric mucus. *Biomaterials* **18**, 677-681, doi:https://doi.org/10.1016/S0142-9612(96)00180-9 (1997).

9 Wagner, C. E. *et al.* Comparison of Physicochemical Properties of Native Mucus and Reconstituted Mucin Gels. *Biomacromolecules*, doi:10.1021/acs.biomac.2c01016 (2023).

10 Sharma, A. *et al.* Polyglycerol-Based Mucus-Inspired Hydrogels. *Macromolecular Rapid Communications* **42**, 2100303, doi:https://doi.org/10.1002/marc.202100303 (2021).

11 Detwiler, R. E. & Kramer, J. R. Preparation and applications of artificial mucins in biomedicine. *Current Opinion in Solid State and Materials Science* **26**, 101031, doi:https://doi.org/10.1016/j.cossms.2022.101031 (2022).

12 Zacco, E. *et al.* Tailored Presentation of Carbohydrates on a Coiled Coil-Based Scaffold for Asialoglycoprotein Receptor Targeting. *ACS Chemical Biology* **10**, 2065-2072, doi:10.1021/acschembio.5b00435 (2015).

13 Zacco, E. *et al.* A Self-Assembling Peptide Scaffold for the Multivalent Presentation of Antigens. *Biomacromolecules* **16**, 2188-2197, doi:10.1021/acs.biomac.5b00572 (2015).

14 Hellmund, K. S. *et al.* Functionalized peptide hydrogels as tunable extracellular matrix mimics for biological applications. *Peptide Science* **113**, e24201, doi:10.1002/pep2.24201 (2021).

15 Jorgensen, M. D. & Chmielewski, J. Recent advances in coiled-coil peptide materials and their biomedical applications. *Chemical Communications* **58**, 11625-11636, doi:10.1039/D2CC04434J (2022).

16 Pagel, K. & Koksch, B. Following polypeptide folding and assembly with conformational switches. *Current Opinion in Chemical Biology* **12**, 730-739, doi:https://doi.org/10.1016/j.cbpa.2008.09.005 (2008).

17 Dawson, W. M. *et al.* Coiled coils 9-to-5: rational de novo design of α-helical barrels with tunable oligomeric states. *Chemical Science* **12**, 6923-6928, doi:10.1039/D1SC00460C (2021).

18 Mehrban, N. *et al.* Functionalized α-Helical Peptide Hydrogels for Neural Tissue Engineering. *ACS Biomaterials Science & Engineering* **1**, 431-439, doi:10.1021/acsbiomaterials.5b00051 (2015).

19 Mehrban, N. *et al.* Assessing Cellular Response to Functionalized α-Helical Peptide Hydrogels. *Advanced Healthcare Materials* **3**, 1387-1391, doi:10.1002/adhm.201400065 (2014).

20 Huang, C.-C., Ravindran, S., Yin, Z. & George, A. 3-D self-assembling leucine zipper hydrogel with tunable properties for tissue engineering. *Biomaterials* **35**, 5316-5326, doi:https://doi.org/10.1016/j.biomaterials.2014.03.035 (2014).

21 Hill, L. K. *et al.* Thermoresponsive Protein-Engineered Coiled-Coil Hydrogel for Sustained Small Molecule Release. *Biomacromolecules* **20**, 3340-3351, doi:10.1021/acs.biomac.9b00107 (2019).

22 Heinz, F. *et al.* How chromophore labels shape the structure and dynamics of a peptide hydrogel. arXiv:2310.09142 (2023). <https://ui.adsabs.harvard.edu/abs/2023arXiv231009142H

https://arxiv.org/pdf/2310.09142.pdf>.

23 Luis, A. S. & Hansson, G. C. Intestinal mucus and their glycans: A habitat for thriving microbiota. *Cell Host & Microbe* **31**, 1087-1100, doi:https://doi.org/10.1016/j.chom.2023.05.026 (2023).

24 Dal Colle, M. C. S. *et al.* Linker, loading, and reaction scale influence automated glycan assembly. *Beilstein Journal of Organic Chemistry* **19**, 1015-1020, doi:10.3762/bjoc.19.77 (2023).

25 Guberman, M., Bräutigam, M. & Seeberger, P. H. Automated glycan assembly of Lewis type I and II oligosaccharide antigens. *Chemical Science* **10**, 5634-5640, doi:10.1039/C9SC00768G (2019).

26 Wendeln, C., Heile, A., Arlinghaus, H. F. & Ravoo, B. J. Carbohydrate Microarrays by Microcontact Printing. *Langmuir* **26**, 4933-4940, doi:10.1021/la903569v (2010).

27 Patel, M. K. *et al.* Analysis of the dispersity in carbohydrate loading of synthetic glycoproteins using MALDI-TOF mass spectrometry. *Chemical Communications* **46**, 9119-9121, doi:10.1039/C0CC03420G (2010).

28 Tsai, T.-W. *et al.* Exploring the Synthetic Application of Helicobacter pylori α1,3/4-Fucosyltransferase FucTIII toward the Syntheses of Fucosylated Human Milk Glycans and Lewis Antigens. *ACS Catalysis* **9**, 10712-10720, doi:10.1021/acscatal.9b03752 (2019).

29 Chiu, C. P. C. *et al.* Structural Analysis of the α-2,3-Sialyltransferase Cst-I from Campylobacter jejuni in Apo and Substrate-Analogue Bound Forms. *Biochemistry* **46**, 7196-7204, doi:10.1021/bi602543d (2007).

30 Ober, K. *et al.* Expanding the Scope of Reporting Nanoparticles: Sensing of Lipid Phase Transitions and Nanoviscosities in Lipid Membranes. *Langmuir* **35**, 11422-11434, doi:10.1021/acs.langmuir.9b01372 (2019).

31 Volz, P. *et al.* White-Light Supercontinuum Laser-Based Multiple Wavelength Excitation for TCSPC-FLIM of Cutaneous Nanocarrier Uptake. *Z. Phys. Chem* **232**, 671-688, doi:10.1515/zpch-2017-1050 (2018).

32 Alexiev, U. & Farrens, D. L. Fluorescence spectroscopy of rhodopsins: Insights and approaches. *Bba-Bioenergetics* **1837**, 694-709, doi:10.1016/j.bbabio.2013.10.008 (2014).

33 Kim, T. Y., Winkler, K. & Alexiev, U. Picosecond multidimensional fluorescence spectroscopy: a tool to measure real-time protein dynamics during function. *Photochem. Photobiol.* **83**, 378-384, doi:10.1562/2006-06-21-RA-943 (2007).

34 Swindells, J. F., Synder, C. F., Hardy, R. C. & Golden, P. E. *Viscosities of Sucrose Solutions at Varoius Temperatures: Tables of Recalculated Values*. (U.S. Government Printing Office, 1958).

35 Vyšniauskas , A. *et al.* Exploring viscosity, polarity and temperature sensitivity of BODIPY-based molecular rotors. *Phys. Chem. Chem. Phys.* **19**, 25252-25259, doi:10.1039/c7cp03571c (2017).

36 Wood, C. W. & Woolfson, D. N. CCBuilder 2.0: Powerful and accessible coiled-coil modeling. *Protein Science* **27**, 103-111, doi:https://doi.org/10.1002/pro.3279 (2018).

37 Case, D. A. *et al.* The Amber biomolecular simulation programs. *Journal of Computational Chemistry* **26**, 1668-1688, doi:https://doi.org/10.1002/jcc.20290 (2005).

38 Danne, R. *et al.* doGlycans–Tools for Preparing Carbohydrate Structures for Atomistic Simulations of Glycoproteins, Glycolipids, and Carbohydrate Polymers for GROMACS. *Journal of Chemical Information and Modeling* **57**, 2401-2406, doi:10.1021/acs.jcim.7b00237 (2017).

39 Curta: A General-purpose High-Performance Computer at ZEDAT, Freie Universität Berlin (2020).

40 Lindorff-Larsen, K. *et al.* Improved side-chain torsion potentials for the Amber ff99SB protein force field. *Proteins: Structure, Function, and Bioinformatics* **78**, 1950-1958, doi:https://doi.org/10.1002/prot.22711 (2010).

41 Pandya, M. J. *et al.* Sticky-End Assembly of a Designed Peptide Fiber Provides Insight into Protein Fibrillogenesis. *Biochemistry* **39**, 8728-8734, doi:10.1021/bi000246g (2000).

42 Rubinstein, M. & Colby, R. H. *Polymer Physics*. (Oxford University Press, 2003).

43 Tschoegl, N. W. *The Phenomenological Theory of Linear Viscoelastic Behavior: An Introduction*. (Springer-Verlag, 1989).

44 Wiechert, E. Gesetze der elastischen Nachwirkung für constante Temperatur. *Annalen der Physik* **286**, 546-570, doi:https://doi.org/10.1002/andp.18932861110 (1893).

45 Applications of Dynamics to Physics and Chemistry. *Nature* **38**, 585-587, doi:10.1038/038585a0 (1888).

46 Tsuji, Y., Li, X. & Shibayama, M. Evaluation of Mesh Size in Model Polymer Networks Consisting of Tetra-Arm and Linear Poly(ethylene glycol)s. *Gels* **4**, 50 (2018).

47 Doi, M. & Edwards, S. F. *The Theory of Polymer Dynamics*. (Clarendon Press, 1986).

48 de Gennes, P. G. *Scaling Concepts in Polymer Physics*. (Cornell University Press, 1979).

49 Pincus, P. Excluded Volume Effects and Stretched Polymer Chains. *Macromolecules* **9**, 386-388, doi:10.1021/ma60051a002 (1976).

50 *CRC Handbook of Chemistry and Physics*. 97 edn, 2670 (CRC Press, 2016).

51 Ruiz-Pulido, G. & Medina, D. I. An overview of gastrointestinal mucus rheology under different pH conditions and introduction to pH-dependent rheological interactions with PLGA and chitosan nanoparticles. *European Journal of Pharmaceutics and Biopharmaceutics* **159**, 123-136, doi:https://doi.org/10.1016/j.ejpb.2020.12.013 (2021).

52 Celli, J. P. *et al.* Rheology of Gastric Mucin Exhibits a pH-Dependent Sol−Gel Transition. *Biomacromolecules* **8**, 1580-1586, doi:10.1021/bm0609691 (2007).

53 Akimoto, M., Hashi, Y. & Suzuki, A. Mean Squared Displacement of a Probe Particle in a Viscoelastic Fluid. *AIP Conference Proceedings* **832**, 545-548, doi:10.1063/1.2204560 (2006).

54 Kalwarczyk, T. *et al.* Comparative Analysis of Viscosity of Complex Liquids and Cytoplasm of Mammalian Cells at the Nanoscale. *Nano Lett* **11**, 2157-2163, doi:10.1021/nl2008218 (2011).

55 Sluch, M. I., Somoza, M. M. & Berg, M. A. Friction on small objects and the breakdown of hydrodynamics in solution: Rotation of anthracene in poly(isobutylene) from the small-molecule to polymer limits. *J Phys Chem B* **106**, 7385-7397, doi:10.1021/jp025549u (2002).

56 Boreham, A. *et al.* Temperature and environment dependent dynamic properties of a dendritic polyglycerol sulfate. *Polym. Adv. Technol.* **25**, 1329-1336, doi:10.1002/pat.3355 (2014).

57 Boreham, A., Brodwolf, R., Walker, K., Haag, R. & Alexiev, U. Time-Resolved Fluorescence Spectroscopy and Fluorescence Lifetime Imaging Microscopy for Characterization of Dendritic Polymer Nanoparticles and Applications in Nanomedicine. *Molecules* **22**, E17, doi:10.3390/molecules22010017 (2016).

58 Boreham, A. *et al.* Detecting and Quantifying Biomolecular Interactions of a Dendritic Polyglycerol Sulfate Nanoparticle Using Fluorescence Lifetime Measurements. *Molecules* **21**, E22, doi:10.3390/molecules21010022 (2015).

59 Akesson, E., Sundstrom, V. & Gillbro, T. Solvent-Dependent Barrier Heights of Excited-State Photoisomerization Reactions. *Chem. Phys. Lett.* **121**, 513-522, doi:Doi 10.1016/0009-2614(85)87132-3 (1985).

60 Brodwolf, R. *et al.* Faster, sharper, more precise: Automated Cluster-FLIM in preclinical testing directly identifies the intracellular fate of theranostics in live cells and tissue. *Theranostics* **10**, 6322-6336, doi:10.7150/thno.42581 (2020).

61 Stennett, E. M. S., Ciuba, M. A., Lin, S. & Levitus, M. Demystifying PIFE: The Photophysics Behind the Protein-Induced Fluorescence Enhancement Phenomenon in Cy3. *J Phys Chem Lett* **6**, 1819-1823, doi:10.1021/acs.jpclett.5b00613 (2015).

62 Sundström, V. & Gillbro, T. Excited state dynamics and photophysics of aggregated dye chromophores in solution. *J. Chem. Phys.* **83**, 2733-2743, doi:10.1063/1.449275 (1985).

63 Schlaich, A., Kappler, J. & Netz, R. R. Hydration Friction in Nanoconfinement: From Bulk via Interfacial to Dry Friction. *Nano Letters* **17**, 5969-5976, doi:10.1021/acs.nanolett.7b02000 (2017).